Size Effects In Plain-Weave Astroquartz® Deployable Thin Shells

Journal of Composite Materials
XX(X):1–15

DOI: 10.1177/ToBeAssigned
www.sagepub.com/
SAGE

Serena Ferraro and Sergio Pellegrino

Abstract

The general scaling trend for brittle materials, in which the strength increases when the sample size decreases, is reversed in plain-weave laminates of Astroquartz® and cyanate ester resin. Specifically, both the shear stiffness and the compressive strength decrease for test samples with widths smaller than 15 times the wavelength of the fabric, and observations at the microscale explain this behavior. The derived scaling is applied to the analysis of a deployable thin shell forming a 90° corner hinge with five cutouts on each side. The cutouts leave narrow strips of material with width as small as one fabric wavelength (1 mm), forming structural ligaments whose strength and stiffness are subject to strong size-scaling effects. A numerical simulation of the folding process followed by a failure analysis is presented, using two alternative material models and failure criteria. The size independent model predicts that the structure will remain damage-free after it is folded and deployed, whereas the size-scaled model predicts that failure will occur. The correctness of the size-scaled model prediction is verified by measuring localized damage in a physical prototype, using x-ray CT scans.

Keywords

size-scaling, plain-weave composites, deployable thin shells, digital volume correlation, x-ray computed tomography

1 Introduction

This study is motivated by recent advances in deployable thin shell structures in which cutouts are introduced to facilitate folding and to achieve desirable snap-back behavior at the end of deployment (Miura and Pellegrino 2020). The regions near the cutouts are subject to high strain and the object of this study is to carry out a detailed material failure analysis of these regions.

Recent studies of thin shell deployable structures with cutouts include Greschik (1996) and Tibbalds et al. (2004), which introduced cutouts in parabolic dishes to allow tight packaging. Tan and Pellegrino (2006, 2012) introduced long and narrow cutouts (slits) along the seam between a parabolic dish and a stiffening rim, to allow the rim to fold elastically. Yee and Pellegrino (2005b); Mobrem and Adams (2009); Mallikarachchi and Pellegrino (2011) made self-deployable and self-latching hinges by introducing parallel cutouts in thin-walled composite cylindrical shells, forming a set of parallel tape springs that allow the hinge to elastically fold, deploy and self-latch.

Studies of the strain distribution near cutouts, in the folded configuration of such structures, show small regions of very high strain but previous studies have not analyzed in detail the true magnitude and effect of these high strain concentrations. However, there has been evidence of cracks forming and propagating through the structures (Mallikarachchi and Pellegrino 2014).

As an example, Fig. 1 shows the numerically predicted rapidly varying distribution of the mid-plane strain ϵ_{11} (where the 1-direction is along the longitudinal axis of the shell) reproduced from Ferraro (2020) in a thin-walled shell forming a 90° corner. An elastic hinge has been formed by introducing five cutouts on each side of the shell, the width of these narrow strips of material ranges from 3 mm to 1 mm. The hinge has been folded 45° and the strains in this folded configuration have been plotted on the undeformed configuration of the structure. The figure shows strain localization by up to 10 times on the edges and

Graduate Aerospace Laboratories, California Institute of Technology, USA

Corresponding author:
Sergio Pellegrino, Graduate Aerospace Laboratories, California Institute of Technology, 1200 E. California Boulevard MS 105-05, Pasadena, CA 91125, USA.

Email: sergiop@caltech.edu

ends of the narrow strips of material formed by the cutouts. The highest strain, marked by a red contour in Fig. 1, is concentrated in an area measuring less than 0.2 mm^2.

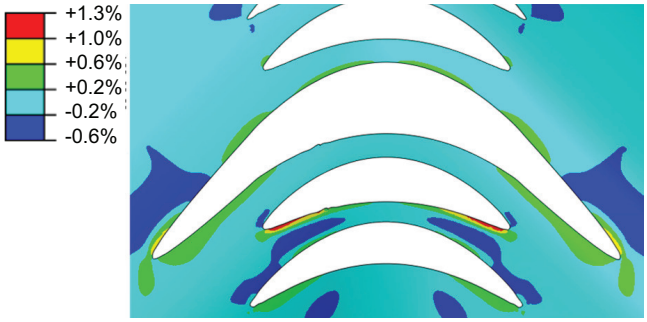

Figure 1. Contour plot of longitudinal strain ϵ_{11} in center region of corner hinge with multiple cutouts. The shell has been folded 45° and the strains are mapped on the deployed configuration.

An analysis of these strain concentrations, which considers both the changes in stiffness and the failure properties of the composite material near the cutouts is presented in this paper.

For a broader perspective about this problem, it should be noted that the effect of scale on the stiffness and strength of solids is a problem of continuing research interest (Bažant and Chen 1999). Both a statistical approach based on Weibull distributions (Weibull 1939; Bullock 1974; Wang et al. 1980; Zweben 1981; Wisnom 1991) and a fracture mechanics approach (Atkins and Caddell 1974; Carpinteri and Bocca 1987; Bažant et al. 1999) have been used to analyze scale effects on the strength of fiber-reinforced composite materials. A comprehensive review of both statistical and deterministic size effects has been provided by Bažant and Le (2017).

The application of the statistical approach is based on the assumption that larger specimens will inherently exhibit a higher number of imperfections, causing a reduction in nominal strength. A concise formulation of this theory (Bullock 1974) yields the result:

$$\frac{\sigma_m^c}{\sigma_p^c} = \left(\frac{V_p}{V_m}\right)^{\frac{1}{\beta}} \tag{1}$$

where the subscripts m and p refer to laboratory scale model and full-scale prototype, respectively; σ^c is the ultimate stress; V is the volume of the sample; β is a parameter that provides a measure of the scatter in the strength data.

A fracture mechanics model (Atkins and Caddell 1974) describes the size-strength relationship for notched, brittle, and isotropic materials with the equation:

$$\frac{\sigma_m^c}{\sigma_p^c} = \sqrt{\lambda} \tag{2}$$

where λ is a geometric scaling parameter, defined as the ratio of the prototype length to the model length.

Jackson et al. (1992) compared these models to experimental results obtained from graphite-epoxy laminates under both tension and bending. The laminates used in their experiments consisted of unidirectional plies arranged in different stacking sequences, chosen to highlight individual and interacting failure modes. Figure 2 shows a plot of the results for cross-ply laminates, $[+45_n/-45_n/+45_n/-45_n]_s$ where the subscript n indicates the number of plies used in one orientation, under bending. The smallest samples, of AS4/3502 graphite-epoxy, were 12.7 mm wide with 8 plies (n = 1).

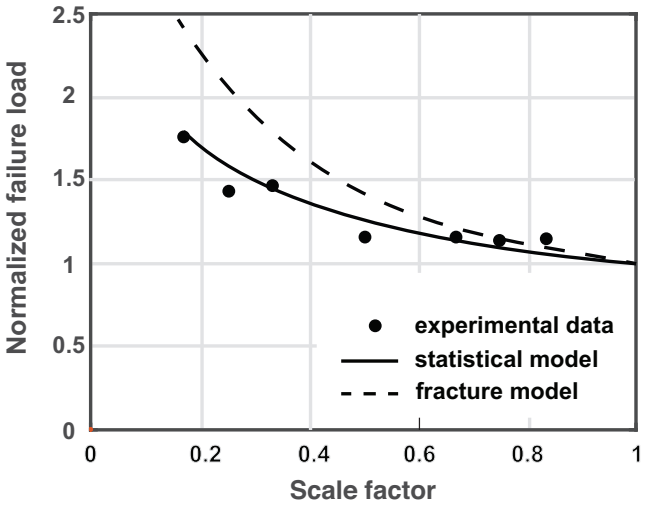

Figure 2. Jackson et al. (1992) compared the normalized failure load versus scale factor with statistical and fracture mechanics models for graphite-epoxy cross-ply samples from 50.8 mm wide and 32 plies (Scale Factor = 1) to 12.7 mm wide and 8 plies (Scale Factor = 0.19), tested in bending.

These results, as well as the published literature on size-scaling of the strength of brittle materials, including fiber-reinforced composites (Weibull 1939; Bullock 1974; Jackson et al. 1992; Bažant and Chen 1999), indicate that there is an increase in strength at smaller scales. Several examples can be found in Bažant (2019).

The present study shows experimentally that the shear strength ±45 plain weave Astroquartz® follows a different size-scaling trend than previously studied materials. Its initial increasing trend is reversed to a decreasing trend for samples narrower than 15 weave wavelengths, and becomes smaller than the strength of the pure resin for sample widths smaller than 2 wavelengths. Observations at a microstructural level explain this trend. In parallel, an experimental characterization of the shear stiffness of this composite material shows a somewhat slower, but still

significant decrease from the full value at 15 wavelengths down to 50% at 1 wavelength.

The implications of these scaling results for the design of deployable shell structures with cutouts are significant. Because of the more rapid decreases in the shear strength than the stiffness, a detailed analysis that accounts for material non-linearity as well actual strength near a cutout may predict failure in cases where a less detailed analysis would have predicted no failure. This is demonstrated through the analysis of a specific shell structure and is verified by direct measurement of residual damage after folding and unfolding a prototype shell structure made of plain weave Astroquartz®.

The paper is organized as follows. The next section introduces the composite material system that is the object of the present study, and lists the relevant mechanical properties. It then determines its macro-scale stiffness and strength parameters, though a combination of analytical and experimental methods. Section 3 presents the size-scaling variation of the stiffness and strength parameters and also provides an explanation for the observed variation. Section 4 analyzes an exemplar deployable shell structure with cutouts, using two alternative material models and failure criteria. The size-scale independent model predicts that the structure will remain damage-free after it is folded and deployed, whereas the size-scaled model predicts that failure will occur. Section 5 presents an experimental verification that damage in this shell structure does indeed occur, using images of the micro-scale from which the residual strains after folding and deployment are shown to be well above the noise threshold of the measurements. Section 6 concludes the paper.

2 Macroscale Stiffness and Strength Parameters

The material used in the present study is plain-weave 525 Astroquartz® II fabric, supplied by JPS Composite Materials (JPS 2017), pre-impregnated with PMT-F6 cyanate ester resin by PATZ Materials & Technologies (PATZ 2019). Its properties, obtained from the suppliers' datasheets (JPS 2017; PATZ 2019), are listed in Table 1. The fabric is a weave of 50 fiber yarns, with a wavelength (measured by the present authors, on cured laminates) of 1 mm.

Table 2 lists the measured thickness of each laminate, cured in an autoclave on a flat mandrel. The next sub-sections present the laminate stiffness and strength properties at the macroscale.

Fibers	
$E_{1f} = E_{2f}$	72 GPa
ν_{12f}	0.16
G_{12f}	31 GPa
diameter	9 μm
Matrix	
E_m	3.64 GPa
ν_m	0.35
G_m	1.35 GPa
Fabric and Cured Lamina	
V_f	0.62
Fabric thickness	80 μm
Areal density (dry)	68 gsm
Wavelength	1 mm

Table 1. Astroquartz® fiber and cyanate ester matrix properties.

Laminate		Thickness (μm)
1 ply		90
2 plies	$[45_{pw}]_2$	160
3 plies	$[45_{pw}/0_{pw}/45_{pw}]$	230
4 plies	$[45_{pw}]_4$	280
6 plies	$[45_{pw}/45_{pw}/0_{pw}]_s$	390

Table 2. Thickness of laminates.

2.1 Stiffness

A linear elastic model of plain-weave Astroquartz® laminates was obtained from Classical Lamination Theory (CLT) (Daniel and Ishai 1994) and micromechanical models for woven composites (Soykasap 2006), combined with experimental results.

The 6×6 $\boldsymbol{ABD}$ stiffness matrix relates the stress resultants per unit width, forces and moments $\boldsymbol{N}$ and $\boldsymbol{M}$, to the mid-plane strains and out-of-plane curvatures, $\boldsymbol{\epsilon}$ and $\boldsymbol{\kappa}$, respectively:

$$\begin{bmatrix} \boldsymbol{N} \\ \boldsymbol{M} \end{bmatrix} = \begin{bmatrix} \boldsymbol{A} & \boldsymbol{B} \\ \boldsymbol{B} & \boldsymbol{D} \end{bmatrix} \begin{bmatrix} \boldsymbol{\epsilon} \\ \boldsymbol{\kappa} \end{bmatrix} \tag{3}$$

Since all of the laminates considered were symmetric, the $\boldsymbol{B}$ matrix is null.

Following Soykasap (2006), the longitudinal modulus and major Poisson's ratio of the tows were calculated using the rule of mixtures (Daniel and Ishai 1994):

$$E_1 = V_f E_{1f} + (1 - V_f) E_m \tag{4}$$

$$\nu_{12} = V_f \nu_{12f} + (1 - V_f) \nu_m \tag{5}$$

The transverse modulus and the in-plane shear modulus were obtained from the Halpin-Tsai semiempirical relations (Haplin and Tsai 1969) as:

$$E_2 = \frac{E_m(1+\xi\eta_E V_f)}{1-\eta_E V_f} \tag{6}$$

$$G_{12} = \frac{G_m(1+\xi\eta_G V_f)}{1-\eta_G V_f} \tag{7}$$

with:

$$\eta_E = \frac{E_{2f}-E_m}{E_{2f}+\xi E_m} \tag{8}$$

$$\eta_G = \frac{G_{12f}-G_m}{G_{12f}+\xi G_m} \tag{9}$$

where it was assumed ξ = 1, as standard for laminates with high fiber volume fraction.

Finally, the minor Poisson's ratio of the yarn was calculated from the reciprocity relationship:

$$\nu_{21} = \nu_{12}\frac{E_2}{E_1} \tag{10}$$

The thickness of each tow was assumed to be half the thickness of a single plain-weave lamina. Hence, the homogenized material properties of a lamina were obtained from the rule of mixtures, assuming that half the fibers are in the longitudinal direction while the other half are in the transverse direction. For example, the longitudinal modulus was calculated as:

$$E_1 = E_2 = 0.5V_f E_{1f} + (1-V_f)E_m \tag{11}$$

Using the tow properties described above, the mosaic model (Soykasap 2006) was used to estimate the $\boldsymbol{A}$ matrix for each of the four laminates. For example, the matrix for the thinnest laminate, $[45_{pw}]_2$, is:

$$\boldsymbol{A}_{[\mathbf{45_{pw}}]_\mathbf{2}} = \begin{bmatrix} 3403.2 & 1872.0 & 0 \\ 1872.0 & 3403.2 & 0 \\ 0 & 0 & 2150.3 \end{bmatrix} \text{(N/mm)} \tag{12}$$

The bending stiffness matrix, $\boldsymbol{D}$, was calculated with the mosaic model and each term was divided by a reduction factor α that accounts for the over-prediction by the mosaic model for small numbers of plies (Soykasap 2006).

The reduction factor is defined as:

$$\alpha = \frac{D_{11_{mosaic}}}{D_{11_{expt}}} \tag{13}$$

where $D_{11_{expt}}$ was obtained from four-point bending tests, see Table 3. As expected, the gap between the prediction made with micromechanical models and the experimental results decreases as the number of plies increases. It should be noted that this correction has no relation with size scaling. In fact, it is mostly due to a mismatch between the geometry assumed by the mosaic model, which neglects the undulation in the yarns and introduces discontinuities in the fibers, and the actual, three-dimensional geometry of plain-weave laminates (Soykasap 2006). Because the geometric effects that cause the coefficient $D_{11_{expt}}$ to be over-predicted by the mosaic model are related to the out-of-plane bending and twisting stiffnesses of the laminate, recent research has assumed a single reduction factor for the whole $\boldsymbol{D}$ (Sakovsky and Pellegrino 2019). A higher-fidelity model, based on a three-dimensional representative volume element, that does not use a reduction factor was used in Mallikarachchi and Pellegrino (2011).

Laminate	Average $D_{11_{expt}}$	Samples	Standard Deviation	α
$[45_{pw}]_2$	3.1	3	0.26	2.34
$[45_{pw}/0_{pw}/45_{pw}]$	10.0	5	0.34	2.19
$[45_{pw}]_4$	23.0	5	1.10	1.69
$[45_{pw}/45_{pw}/0_{pw}]_s$	69.8	5	1.30	1.30

Table 3. Bending stiffness D_{11} (Nmm) and reduction factor α for two- to six-ply laminates.

Using the experimental results, correction factors were calculated for each layup, Eq. (13), and were applied to every term of the $\boldsymbol{D}$ matrix, while matrices $\boldsymbol{A}$ and $\boldsymbol{B}$ were left unchanged. For example, the $\boldsymbol{D}$ matrix for the two-ply laminate $[45_{pw}]_2$ is:

$$\boldsymbol{D}_{[\mathbf{45_{pw}}]_\mathbf{2}} = \begin{bmatrix} 3.10 & 1.71 & 0 \\ 1.71 & 3.10 & 0 \\ 0 & 0 & 1.96 \end{bmatrix} \text{(Nmm)} \tag{14}$$

2.2 Strength

Failure predictions were made using a laminate failure criterion for ultra-thin, plain-weave composites (Mallikarachchi and Pellegrino 2013). The criterion applies to layups with same orientation plies and uses three non-dimensional failure indices to capture in-plane, bending, and coupled in-plane and bending failure. The failure indices are defined as follows:

$$FI_1 = f_1(N_x+N_y) + f_{11}(N_x^2+N_y^2) + f_{12}N_xN_y + f_{33}N_{xy}^2 < 1 \tag{15}$$

$$FI_2 = f_{44} \times \max(M_x^2, M_y^2) + f_{66}M_{xy}^2 < 1 \tag{16}$$

$$FI_3 = \max\left(\frac{N_x}{F_x}, \frac{N_y}{F_y}\right) + \frac{\max(|M_x|, |M_y|)}{F_4} < 1 \quad (17)$$

where the failure coefficients, f_i and f_{ij}, are given by:

$$f_1 = f_2 = \frac{1}{F_{1t}} - \frac{1}{F_{1c}} \quad (18a)$$

$$f_{11} = f_{22} = \frac{1}{F_{1t}F_{1c}} \quad (18b)$$

$$f_{12} = -\frac{f_{11}}{2} \quad (18c)$$

$$f_{33} = \frac{1}{F_3^2} \quad (18d)$$

$$f_{44} = f_{55} = \frac{1}{F_4^2} \quad (18e)$$

$$f_{66} = \frac{1}{F_6^2} \quad (18f)$$

The terms F_i represent directly measured or calculated strengths in the tow directions of the laminate, and the subscripts t and c denote tension and compression, respectively.

For both tensile and compressive strengths the subscripts 1 and 2 refer to the directions parallel and perpendicular to the fibers, respectively. Hence, for a plain-weave laminate $F_{1t} = F_{2t}$ and $F_{1c} = F_{2c}$.

The tensile strength was measured as the smallest stress resultant at failure measured from tension tests on $[0_{pw}]_2$ and $[0_{pw}]_4$ laminates. 15 mm wide test samples were pulled under tension at a rate of 2 mm/min until failure, according to ASTM (2009).

The compressive strength was calculated using elasto-plastic fiber microbuckling theory (Fleck and Budiansky 1991):

$$F_{1c} = \frac{G}{1 + \frac{\phi_0}{\gamma_y}}t \quad (19)$$

where ϕ_0 is the fiber misalignment angle, γ_y is the in-plane yield shear strain, and t is the tow thickness. γ_y was derived from direct measurements of the shear strength τ_y, with

$$\gamma_y = \frac{\tau_y}{G} \quad (20)$$

and G is the shear modulus of a composite tow

$$G = \frac{G_m(G_{12f} + G_m + V_f(G_{12f} - G_m))}{G_{12f+G_m-V_f(G_{12f}-G_m)}} \quad (21)$$

The fiber misalignment angle was measured from micrographs of one, two, and four ply plain-weave laminates, as shown in Fig. 3.

The in-plane shear strength, F_3, was measured as the smallest failure value obtained from tension tests on $[45_{pw}]_2$ and $[45_{pw}]_4$ laminates:

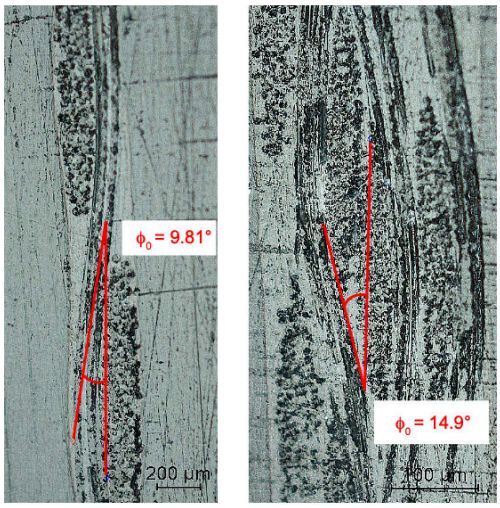

Figure 3. Micrographs of one- and four-ply plain weave Astroquartz® laminates showing measurements of fiber misalignment angle, ϕ_0.

$$F_3 = N_{xy} = \cos\alpha \sin\alpha N_{x'} = \frac{1}{2}N_{x'} \quad (22)$$

where x' is the loading direction, x and y are the fiber directions, and α = 45° is the fiber orientation angle. The test samples were 15 mm wide and were pulled at a rate of 2 mm/min until failure, according to ASTM (2007). It should be noted that, since this test does not apply a pure shear, the value of the shear strength neglects the effects of the applied tension.

A typical shear response, obtained by applying the transformation in Eq. 22 to the measurements, is shown in Fig. 4. The plot shows a first region where the shear stress resultant vs. strain response has the highest slope, followed by a second region of lower slope. Finally, the slope increases again and remains approximately constant until failure. This behavior is characteristic of toughened interface systems (Nguyen et al. 2019). The lower slope in the second region is associated with matrix shear cracks and the length of this region depends on the evolution of macro-cracking, finally reaching a saturated state. Hence, the material under study behaves as a toughened interface system, which exhibits intralaminar micro-cracking and macro-cracking, thus delaying the onset of delamination and prolonging the ultimate failure. This behavior could be explained by the three-dimensional pattern of the plain-weave, which acts as the particles dispersed within the resin-rich regions of a toughened interface system.

The bending strength, F_4, was obtained from the smallest failure moment measured from platen bending tests

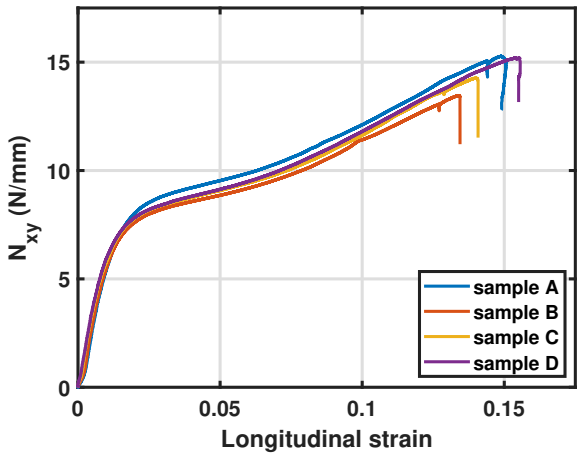

Figure 4. Typical shear response of two-ply laminate.

(Mallikarachchi and Pellegrino 2013; Yee and Pellegrino 2005a; Murphey et al. 2015) on $[0_{pw}]_2$ and $[0_{pw}]_4$ laminates.

Lastly, the twisting strength, F_6, was obtained from the smallest failure moment measured from platen bending tests of $[45_{pw}]_2$ and $[45_{pw}]_4$ laminates:

$$F_6 = M_{xy} = \cos\alpha \sin\alpha M_{x'} = \frac{1}{2} M_{x'} \qquad (23)$$

It should be noted that, since this test does not apply a pure twisting moment, the value of the twisting strength neglects the effects of the applied bending moment.

Table 4 summarizes the strength parameters for two-ply and four-ply laminates.

Strength Parameter	Average Value	Samples	Standard Deviation
Two-ply laminates			
$F_{1t} = F_{2t}$ (N/mm)	76.16	5	2.83
$F_{1c} = F_{2c}$ (N/mm)	34.50	-	-
F_3 (N/mm)	14.55	5	0.12
F_4 (N)	3.26	4	0.28
F_6 (N)	1.10	4	0.06
Four-ply laminates			
$F_{1t} = F_{2t}$ [N/mm]	150.00	4	1.47
$F_{1c} = F_{2c}$ [N/mm]	65.69	-	-
F_3 (N/mm)	30.88	5	0.21
F_4 (N)	8.78	4	1.28
F_6 (N)	3.65	4	0.10

Table 4. Macroscale strength parameters for two-ply and four-ply laminates.

3 Size-Scaling of Stiffness and Strength

Samples with seven different widths, in the range 25 mm to 1 mm, were laser cut to replicate the manufacturing procedure used to form cutouts in deployable shell structures. The samples were tested to characterize their stiffness and strength in shear, by loading them in tension at 45° to the fiber directions. The dimensions of the samples were scaled according to ASTM (2007, 2009). The samples had uniform, rectangular cross-section and a minimum length defined by the sum of the grip length (2×10 mm), two times the width of the sample, and gauge length (11 mm). The width tolerance was ±1%. Figure 5 shows the test setup. Five to ten samples of each width were built and tested. Only tests in which failure occurred within the gauge length, as shown for a 1.5 mm wide sample in Fig. 5, were considered successful.

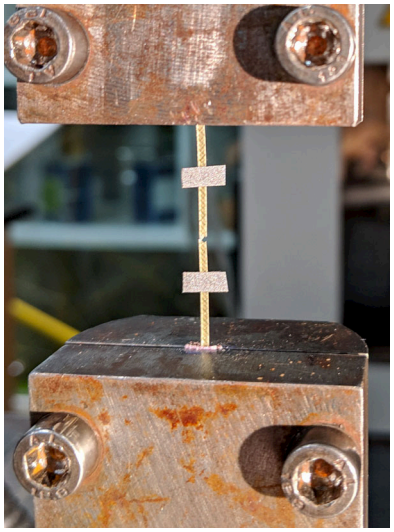

Figure 5. Tension test setup, with 1.5 mm wide sample that has failed within the gauge length.

Average shear stress resultant curves for two-ply samples of widths in the range 15 mm to 1 mm, plotted against the longitudinal strain, are shown in Fig. 6. Size-scaling effects are very noticeable. Specifically, the initial slope (stiffness), maximum stress resultant and strain at failure decrease with the width of the samples. Note that the shear strength of 1 mm wide samples is approximately one third of the shear strength of the 15 mm wide samples.

The measured shear strengths have been plotted in Fig. 7, which displays two different size-scaling trends. For widths of 25 mm to 15 mm the test data shows an increase in strength as the width decreases, following the general trend of theoretical and experimental studies of size effects on the strength of brittle materials (Weibull 1939; Bullock 1974; Jackson et al. 1992; Bažant and Chen 1999; Bažant 2019). For widths of 15 mm to 1 mm the trend reverses and the shear strength decreases as the width of the samples is decreased. In particular, note that the shear strength of 1 mm wide samples is lower than the shear strength of unreinforced cyanate ester resin.

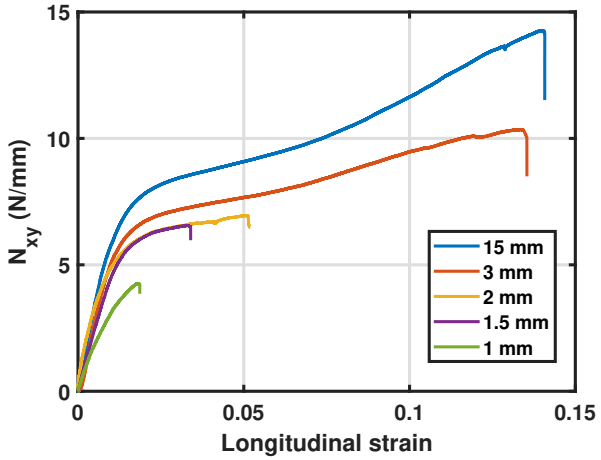

Figure 6. Average shear stress resultant curves for $[45_{pw}]_2$ laminates of different widths, plotted against the longitudinal strain.

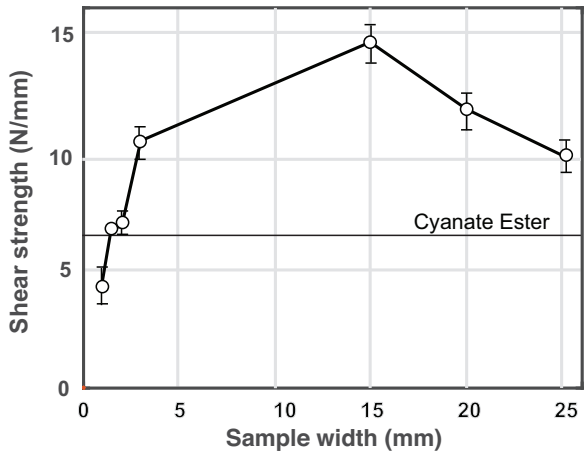

Figure 7. Shear strength scaling of $[45_{pw}]_2$ laminates. The strength of pure cyanate ester resin has been plotted for reference.

Size scaling of the stiffness of the test samples was studied by analyzing the small strain shear response, Fig. 8. Here, the stress resultant vs. strain responses were approximated with straight lines and the slopes of these lines showed a monotonic decreasing trend for decreasing width of the samples. Note that two of the five curves plotted in Fig. 8 show a lower stiffness near the origin, due to a small amount of initial slackness in the tests.

This behavior corresponds to a reduction of the shear stiffness of the material at a scale of less than 15 mm, and was modeled by introducing a shear stiffness scaling factor, β, defined as the ratio between the measured stiffness and the coefficient A_{66} in section 2.1. The values of β for different widths are presented in Table 5.

A further scaling effect needs to be considered. Because the compressive strength is related to the yield shear stress, through Equations 19-21, the compressive strength F_{1c} must also be scaled to account for the reduction in the shear

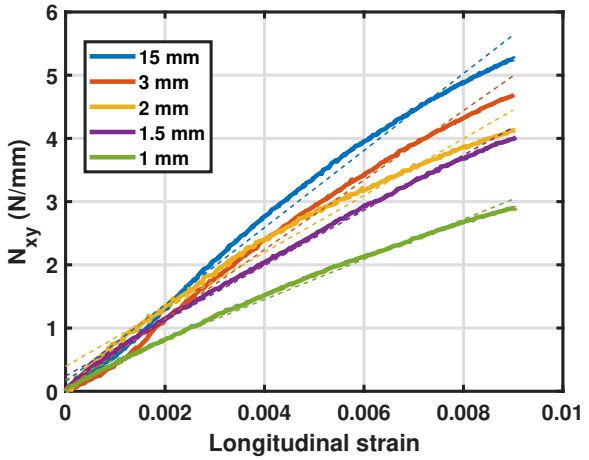

Figure 8. Initial part of shear stress curves and trend lines showing stiffness scaling.

Sample Width (mm)	Shear Strength F_3 (N/mm)	Compressive Strength F_{1c} (N/mm)	Stiffness Scaling Factor β
15	14.55	34.50	1
3	10.34	29.07	0.902
2	6.91	25.94	0.739
1.5	6.76	25.70	0.717
1	4.27	19.37	0.520

Table 5. Size-scaling of shear strength, compressive strength, and stiffness of $[45_{pw}]_2$ Astroquartz ® laminates.

stiffness and the yield shear stress. The resulting scaling of the compressive strength has been included in Table 5.

In conclusion, it has been shown that both the shear strength and stiffness of Astroquartz® and cyanate ester resin laminates decrease with decreasing width in the range 15 mm to 1 mm, as shown in Table 5. Since the wavelength of the Astroquartz® fabric is 1 mm, the sample widths in the first column of the table are in fact equal to the number of wavelengths.

These experimental results can be explained by three microscale effects:

1. The in-plane stiffness of a woven material is decreased by the presence of free edges. This effect can be understood by modeling the material as a two-dimensional lattice of finite width, whose axial stiffness increases asymptotically towards the stiffness of the infinite lattice (Aoki and Yoshida 2006; Fan et al. 2009).
2. Edge effects due to dry spots in the laminates. This is a common type of imperfection in pre-impregnated composites with high fiber volume ratio (V_f = 0.62). When the laser beam cuts through a dry spot, the void

between consecutive weaves of fibers is exposed, thus creating a notch on the edge.

3. Fiber pull-out due to short fibers. Near the edges and cutouts only a short length of fiber is embedded in the matrix, and hence the fibers can more easily be pulled out of the surrounding matrix when a tension load is applied.

Figures 9 and 10 show two images of a 3 mm wide Astroquartz® and cyanate ester sample, $[45_{pw}]_2$, taken with a Nikon Eclipse LV150N microscope with a Nikon TU Plan Fluor 5X/0.15 objective lens set at a magnification of 5X and a numerical aperture of 0.15. The exposure time was 7.9 ms. The edges of the thin strip of composite material had been laser cut and the two photos show the edge of the same sample at two different locations. While in Fig. 9 there is no visible imperfection near the edge, Fig. 10 shows many imperfections.

Circled in red in Fig 10 is a notch on the edge of the laminate. This type of defect appears frequently along the edges. It is caused by the laser beam cutting through a dry spot and exposing the void between consecutive weaves of fibers. These edge defects measure tens of microns, and can propagate and cause premature failure of the sample under tension. These effects are particularly important when testing samples only a few millimeters wide.

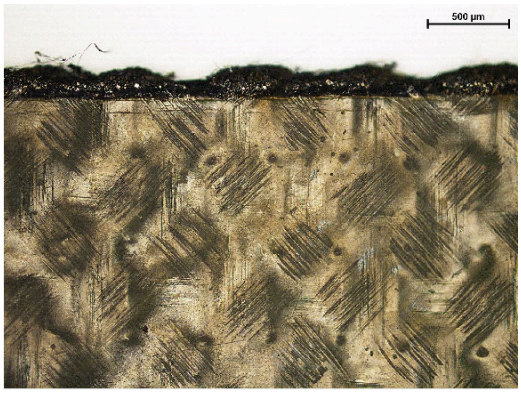

Figure 9. Edge of 3 mm wide, laser cut laminate without visible defects.

Another effect that needs to be taken into account is fiber pull-out. Fibers oriented at $\pm 45°$, in samples that are 3 mm wide or less, can only be as long as 4.25 mm. There are no fibers running through the entire length of these narrow samples, as it would happen if the fibers were oriented at $0°$. Hence, when these samples are loaded in tension, bundles of fibers can pull out of the surrounding matrix, thus causing failure of the sample as sketched in Figure 11. This edge effect also introduces additional compliance.

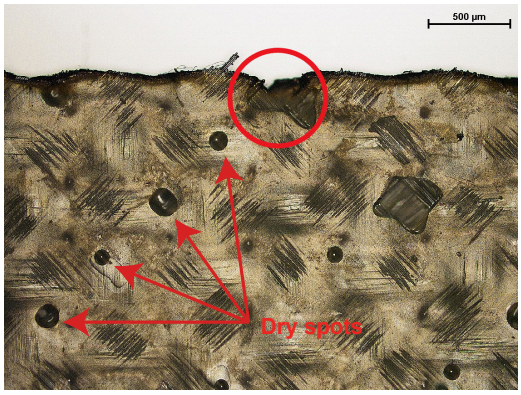

Figure 10. Edge of 3 mm wide, laser cut laminate with defects, mostly due to dry spots.

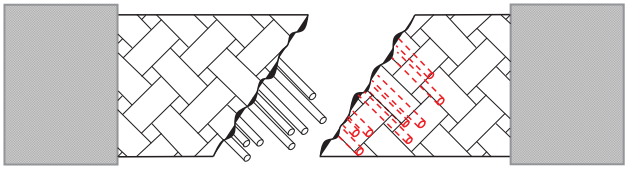

Figure 11. Illustration of fiber pull-out due to short fibers in the samples under study.

4 Introducing Size Effects in Numerical Analysis of Deployable Shells

Geometrically nonlinear simulations of the folding of a deployable thin shell structure forming a corner hinge were carried out with the finite element software Abaqus 2017. The shell geometry was defined by the intersection of two cylindrical surfaces with diameter of 38 mm and axes at $90°$. The outer part of the intersection was rounded with a 14 mm radius and the inner part with a radius of 3 mm. Because in the folded configuration the sides of the corner region are the most highly deformed part of the structure, this part of the structure used the thinnest laminate (two-plies) to minimize the strains induced by bending.

The finite element model consisted of reduced integration S4R quadrilateral shell elements. The simulations were carried out with the Abaqus implicit solver, where after each increment the analysis starts Newton-Raphson iterations to enforce equilibrium of the internal forces with the external loads. Convergence settings based on "half-increment residual tolerance" were used. This tolerance represents the equilibrium residual error (out-of-balance forces) halfway through a time increment. If the half-increment residual is small, it indicates that the accuracy of the solution is

high and that the time step can be increased; conversely, if the half-increment residual is large, the time step used in the solution should be reduced. The Abaqus default half-increment residual tolerance was used, which is set at 1000 times the time average force and moment values.

A folding simulation imposed a relative rotation of 45° between the ends of the cylindrical surfaces, thus increasing the angle between them from 90° to 135°. At the end of the simulation, the three failure indices in Eqs 15-17 were evaluated in the folded configuration for the central region of the hinge, which is most highly strained. For further details see Ferraro (2020).

Two analyses were carried out. The only difference was that the stiffness and strength parameters, which in the first analysis were based on the macroscale values obtained in section 2, were replaced in the second analysis with the appropriate scaled values.

In the first analysis the macroscale stiffness and strength parameters were used to simulate folding and evaluate the failure criterion. A contour plot of the highest failure index, i.e. the in-plane failure index FI_1 in the two-ply region of the shell is shown in Fig. 12. The highest value of the failure index is 0.85, and hence this analysis predicts that the shell will not be damaged when it is folded.

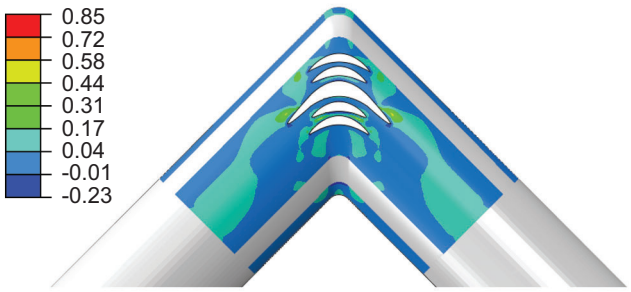

Figure 12. Contours of in-plane failure index, FI_1 over two-ply region of thin shell forming a corner hinge, plotted on undeformed configuration.

In the second analysis the two-ply region of the shell was divided into different sections, as shown in Fig. 13, each corresponding to a different set of stiffness and strength parameters in Table 5. The Abaqus feature "general section properties" was used to input the $\boldsymbol{ABD}$ stiffness matrix of each material section. Size effects were accounted for by modifying the shear stiffness A_{66} depending on the average size of the section. Hence, the $\boldsymbol{A}$ matrix was modified to :

$$\begin{bmatrix} A_{11} & A_{12} & 0 \\ A_{12} & A_{22} & 0 \\ 0 & 0 & \beta A_{66} \end{bmatrix} \tag{24}$$

Also, the scaled failure parameters listed in Table 5 were used for each material section.

Figure 13. Sections of two-ply region simulated with lower stiffness and strength.

A contour plot of the in-plane failure index, FI_1, in the two-ply region of the folded shell is shown in Fig. 14. Black contours correspond to regions where the failure index is smaller than 1. White regions correspond to cutouts or parts of the shell that were excluded from the failure analysis. All of the elements plotted with a color other than white or black have reached a failure index greater than 1, and hence correspond to regions that are predicted to fail. Note that these regions are very small, with an area of approximately 0.2 mm^2.

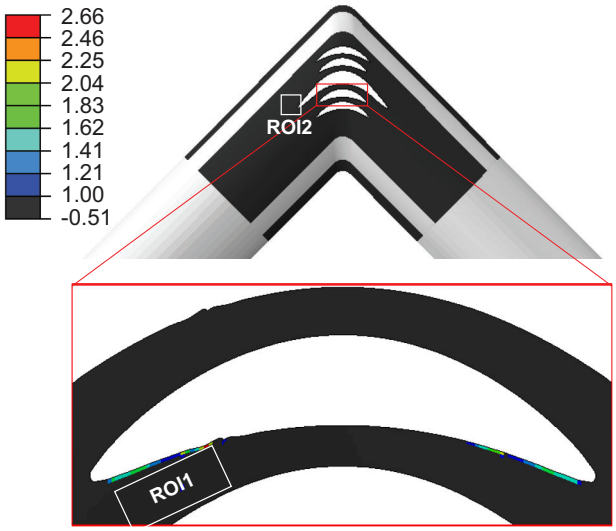

Figure 14. Contour plot of in-plane failure index FI_1 over two-ply region of thin shell forming a corner. Size-scaling effects were included in this analysis. The Regions of Interest ROI1 and ROI2 are discussed in section 5.2.

In conclusion, while the analysis that did not consider size-scaling effects, Fig. 12, showed no signs of damage in the folded shell, the more refined analysis has shown failure in one of the thin strips that separate the cutouts.

However, since the extent of the localized damage predicted by the analysis is five times smaller than the smallest test sample in the size-scaling study in section 3 an experimental verification of this result is in order, and will be presented in the next section.

5 Localized Damage Near Cutouts

X-ray computed tomography (CT) allows imaging of materials in three dimensions with high spatial resolution (Stock 2008; Bale et al. 2013). It combines X-ray measurements of a specific area of a scanned sample, taken from different angles, to produce cross-sectional images, called slices. Using software, the slices are combined to produce a three-dimensional (3D) image.

An example scan of a plain weave Astroquartz® shell with cutouts in the central two-ply region, matching the structure analyzed in section 4, is shown in Fig. 15. A ZEISS Xradia VersaXRM-510 CT scanner was used with the following settings: optical magnification 4X, exposure time 1 s, voltage 80 kV, power 7 W, and number of projections 3001. The area of interest corresponds to the left side of the region with $FI_1 > 1$ in Fig. 14. The slices were reconstructed in a 3D rendering using the software Dragonfly 2019.1. The resolution for the scan shown in Fig. 15 was:

$$1 \text{ voxel} = 4.38\ \mu\text{m} \times 4.38\ \mu\text{m} \times 4.38\ \mu\text{m} \qquad (25)$$

At this setting, the field of view in a single scan is approximately 4.5 mm $\times$ 4.5 mm. In Figs 14 -15 note that ROI1 does not extend all the way to the edge of the sample. This is because the strain data in an outer layer of width equal to the size of the DVC interrogation window is inaccurate.

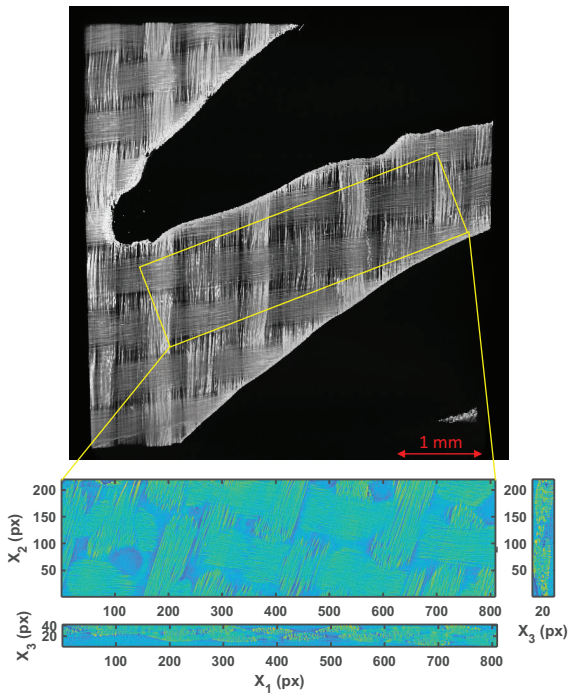

Figure 15. Computed tomography scan of narrow ligament in two-ply, plain-weave laminate thin shell forming a corner hinge.

Strain components are measured via digital volume correlation (DVC) techniques (Xu 2018). DVC is the three-dimensional extension of digital image correlation (DIC), which provides quantitative measurements of the displacement field (Bay 2008). Two tomographic images, a reference image and a target image, are used to estimate the displacement field by finding a unique correspondence between features in the two images.

Since the two-ply laminate used in this study is very thin, the introduction of artificial speckles could both compromise the integrity of the test samples and cause complications in the manufacturing process. Hence, the weave pattern from the laminate itself was used, although it did not provide ideal conditions for correlation and caused measurement noise, as discussed in the next section.

A publicly available MATLAB based software for fast iterative digital volume correlation (FIDVC) (Bar-Kochba et al. 2015) was used to calculate the residual strains after folding and unfolding the shell. This open source software was chosen because it allows for 3D full-field measurement of large-deformation internal displacement fields.

5.1 Measurement Noise and Calibration of DVC Algorithm

A threshold for the measurement noise was estimated by correlating a reference tomographic image and a target image of a flat sample. Both the scan region and the measurement are shown in Fig. 16. The sample has the same layup, $[45_{pw}]_2$, as the region of interest in the deployable shell. A reference image was taken by scanning an area of the sample, shown by a red box in Fig. 16, at the same spatial resolution used to scan the shell. A second image was taken after taking the sample out of the CT scanner and putting it back without applying any strain to it. Hence, the nominal residual strain in the scanned sample was zero everywhere.

The in-plane E_{11} component of the residual strain, calculated on the mid-plane, is shown in Fig. 16. The contour plot shows fictitious residual strains as high as 0.43%. Measurement noise is to be expected in this kind of tomographic images. It is mostly due to inconsistent speckle patterns (Liu and Morgan 2007) and periodicity of the image, due to the pattern formed by the plain-weave, which can lead to mis-registration issues (Sutton et al. 2009).

Also, the process of acquiring different tomographic images by scanning the same sample twice introduces noise. Part of the noise comes from temperature fluctuation within the CT scanner chamber. The most common source of noise from an image acquisition system can be modeled

as Gaussian random noise and conventional noise removal filters are efficient in smoothing the noise (Jain 1989). Therefore, after feeding the two images to the FIDVC algorithm and calculating the residual strain, an additional spatial filter was applied to the strain field. The purpose of the filter is to eliminate high spatial frequency features, using the repeating wavelength of the weave, λ_c, as cutoff value. A low-pass Gaussian filter was implemented as follows:

$$G_{LP}(u,v) = 1 - e^{\frac{-(u^2+v^2)}{2\sigma_c^2}} \tag{26}$$

where u, v are the spatial frequencies in the X_1, X_2 directions, respectively; $\sigma_c = 1/\lambda_c$ defines the width of the Gaussian function and therefore the range of frequencies to be filtered.

To show the effects of the Gaussian filter, two consecutive scans of the same sample were taken. The sample was not removed from the chamber between scans, thus eliminating errors resulting from rigid body motions. The two scans targeted exactly the same volume, and hence no preregistration of the tomographic images was needed.

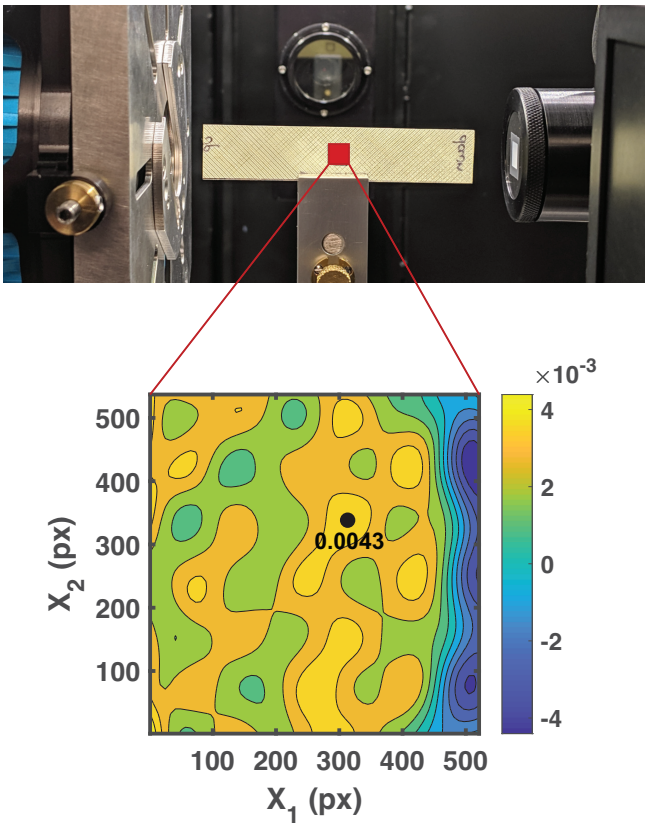

Figure 16. Measurement noise in tomographic images of a flat, unstrained sample, correlated via FIDVC. The contour plot shows the first, in-plane component of the Lagrange strain, E_{11}.

When calibrating the FIDVC algorithm for the 3D images used in this study, the fictitious residual strain was initially in the 15% range. The following key steps were taken to reduce the baseline noise, finally achieving the previously mentioned value of 0.43%:

- **Step 1.** Find correct size of interrogation window and mesh grid spacing using images of numerically deformed sample (no experimental measurement noise).
- **Step 2.** Measure baseline noise from numerical rigid body motion and estimate admissible rigid body displacements. This step helped greatly in reducing rigid body motion between the two tomographic images to an admissible range of less than 10 pixels.
- **Step 3.** Reduce noise from rigid body motion using registration of images by decreasing rigid body offset to an admissible range.
- **Step 4.** Reduce residual noise from experimental measurement using a low-pass Gaussian filter.

By applying steps 1-4 of the calibration procedure, the measurement noise was reduced to the level shown in Fig. 16.

An example high resolution CT scan of a two-ply, plain-weave, flat laminate is shown in Fig. 17. The spatial resolution used to conduct this scan was:

$$1 \text{ voxel} = 0.7\ \mu\text{m} \times 0.7\ \mu\text{m} \times 0.7\ \mu\text{m} \tag{27}$$

While each fiber is well resolved, as can be seen from the tomographic reconstruction of the scanned volume, the field of view is reduced to less than 1 mm.

5.2 Measurement of Damage

Scans of selected areas of a prototype deployable thin shell forming a corner hinge were taken before and after folding the structure. The reference tomographic images, from scans taken before folding the shell, were then correlated to the deformed images, from scans of the same regions of the shell that were taken after folding it. No cracks or any signs of damage were seen in the images. The results obtained for the two regions of interest ROI1 and ROI2 previously identified in Fig. 14, are presented.

Figure 18 shows the residual strain component E_{11} measured in ROI 1. The contour plot of the in-plane component of the Lagrange strain, E_{11}, calculated on the mid-plane of the shell, shows a residual strain as high as 0.81%. This value is almost double the measurement noise of 0.43%, thus indicating that localized damage occurred in this region of the shell when it was folded. This experimental finding is in agreement with the numerical predictions, in

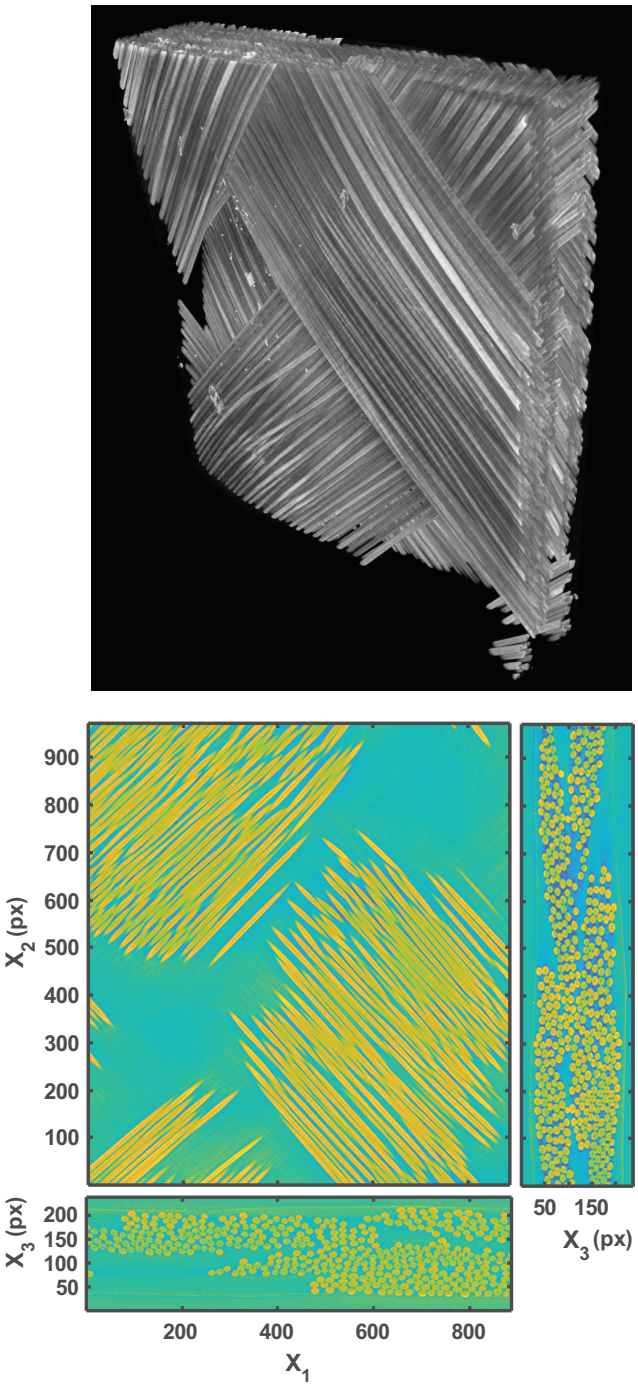

Figure 17. Tomographic reconstruction of CT scan of a two-ply, plain-weave, flat laminate acquired with a spatial resolution of 0.7 μm.

Fig. 14, that localized damage would be caused in this ligament by folding. Note that the size of the areas that are numerically predicted to become damaged and are experimentally showing damage are comparable.

The numerically predicted damage is localized near the edge of the thin strip, in areas measuring approximately 0.2 mm^2, and defined with a spatial resolution of 125 μm, equal to the average finite element size near the cutouts. The highest residual strain that was measured experimentally is also localized near the edge of the thin ligament in an area

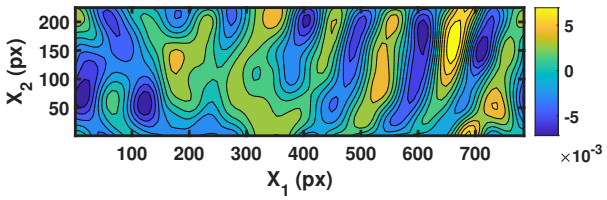

Figure 18. Contour plot of E_{11} component of Lagrange strain resulting from cross-correlation of tomographic images of ROI 1, before and after folding the shell.

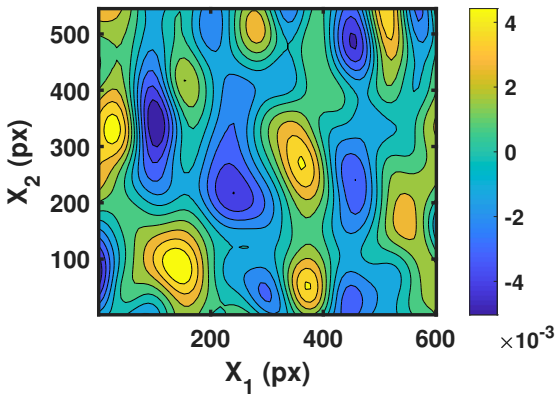

Figure 19. Contour plot of E_{11} component of Lagrange strain resulting from cross-correlation of tomographic images of ROI 2, before and after folding the shell.

measuring approximately 0.04 mm^2, with a spatial resolution of 35 μm.

The spatial resolution of the obtained DIC results is calculated as the product between the spatial resolution of the tomographic images (voxel size) and the mesh grid spacing (Xu 2018) chosen to run the FIDVC algorithm. Since a voxel measures the same length in all three directions, X_1, X_2, and X_3, and the mesh grid spacing is also the same, the spatial resolution is given by:

$$r = px \times dm = 4.38\,\mu\text{m} \times 8 = 35\,\mu\text{m} \qquad (28)$$

where px is the size of the pixel in the tomographic images and dm is the chosen mesh grid spacing for the FIDVC algorithm.

The residual strain in ROI 2 is shown in Fig. 19. The contour plot of the E_{11} component of the Lagrange strain shows a maximum residual strain comparable to the measurement noise value of 0.43%. Hence, for this ROI it is not possible to establish whether localized damage has occurred.

6 Conclusion

This study has found that the general strength scaling trend for brittle materials, in which the strength increases when the sample width decreases, is reversed in plain-weave laminates of Astroquartz® and cyanate ester resin, for sample widths smaller than 15 wavelengths of the fabric. Specifically, both the shear stiffness and the compressive strength decrease in the width range of 15 to 1 wavelengths. These effects are summarized in Table 5.

Two dominating effects at the microscale have been identified. First, edge effects due to dry spots in pre-impregnated composites with high fiber volume ratio. Second, fiber pullout due to the short length of the fibers oriented at $\pm$ 45° with respect to the loading direction.

These results have been applied to the analysis of a deployable thin shell forming a 90° corner hinge with five cutouts on each side of the corner region to allow damage-free folding and snap-back latching at the end of deployment. The cutouts leave narrow strips of material with width as small as one wavelength of the fabric (1 mm), forming structural ligaments whose strength and stiffness are subject to strong size-scaling effects.

For a specific design of this deployable structure, numerical simulations of the folding process have been carried out, initially using a scale-independent stiffness model and the scale-independent failure criterion in (Mallikarachchi and Pellegrino 2013). The results of this analysis predicted that folding the structure would not cause damage anywhere. A more detailed simulation of the same shell structure was then carried out, this time using in the region of the cutouts the scale-dependent stiffness and strength parameters derived in the present study. This more detailed study led to a different outcome, namely that damage would indeed occur in regions of sub-wavelength scale.

This result was verified by measuring the localized damage of a prototype thin Astroquartz® deployable shell structure with the same pattern of cutouts considered in the numerical simulations. Residual strains of 0.81% were measured in a same strip of material using X-ray CT scans scans and digital volume correlation techniques. The magnitude of the residual strains exceeded the baseline measurement noise, thus indicating that localized damage had indeed taken place.

Localized damage in thin-walled composite structures structures may be considered acceptable in some situations, but it may also explain numerous failures that have been reported after multiple fold-deploy cycles of similar structures.

It is concluded that the scaling results measured in the present paper have significant implications for the design of deployable shell structures with cutouts. It has been demonstrated that if size-scaling is not taken into account then the failure analysis can be inaccurate and lead to non conservative predictions.

Acknowledgements

This work was supported by a NASA Space Technology Research Fellowship, with Dr. William Doggett as mentor. The help of Professor Christian Franck, Department of Mechanical Engineering University of Wisconsin-Madison, and his research group in using FIDVC is gratefully acknowledged.

References

Aoki, T. and K. Yoshida (2006). Mechanical and thermal behaviors of triaxially-woven carbon/epoxy fabric composite. 47th AIAA/ASME/ASCE/AHS/ASC Structures, Structural Dynamics and Materials Conference. AIAA-2006-1688

ASTM (2007) Standard test method for in-plane shear response of polymer matrix composite materials by tensile test of a $\pm 45°$ laminate. D3518/D3518M.

ASTM (2008) Standard test method for flexural properties of unreinforced and reinforced plastics and electrical insulating materials by four point bending. D6272-02.

ASTM (2009) Standard test method for tensile properties of polymer matrix composite materials. D3039/D3039M.

Atkins AG and Caddell RM (1974) The laws of similitude and crack propagation. International Journal of Mechanical Sciences 16(8): 541–548.

Bale HA, Haboub A, MacDowell AA, Nasiatka JR, Parkinson DY, Cox BN, Marshall DB and Ritchie RO (2013) Real-time quantitative imaging of failure events in materials under load at temperatures above 1,600 C. Nature Materials 12(1).

Bar-Kochba E, Toyjanova J, Andrews E, Kim KS and Franck C (2015) A fast iterative digital volume correlation algorithm for large deformations. Experimental Mechanics 55(1): 261–274.

Bay BK (2008) Methods and applications of digital volume correlation. Journal of Strain Analysis for Engineering Design 43(8): 745–760.

Bažant ZP (2019) Design of quasibrittle materials and structures to optimize strength and scaling at probability tail: an apercu. Proc. R. Soc. A 475(2018–0617).

Bažant ZP and Chen EP (1999) Scaling of structural failure. Applied Mechanics Reviews ASME 50(10): 383–433.

Bažant ZP, Kim JJH, Daniel IM, Becq-Giraudon E and Zi G (1999) Size effect on compression strength of fiber composites failing

by kink band propagation. International Journal of Fracture 95(103): 1–4.

Bažant ZP and Le JL (2017) Probabilistic Mechanics of Quasibrittle Structures: Strength, Lifetime, and Size Effect. Cambridge University Press.

Bower AF (2011) Applied Mechanics of Solids. CRC Press.

Bullock RE (1974) Strength ratios of composite materials in flexure and in tension. Journal of Composite Materials 8(2): 200–206.

Carpinteri A and Bocca P (1987) Transferability of small specimen data to full-size structural components. Composite Materials Response: Constitutive Relations and Damage Mechanisms : 111–31.

Daniel IM and Ishai O (1994) Engineering Mechanics of Composite Materials, 3rd edition. Oxford University Press, New York.

Fan H, Jin F and Fang D (2009) Characterization of edge effects of composite lattice structures, Composites Science and Technology, 69 (11–12): 1896-1903.

Ferraro, S., 2020. Topology Optimization and Failure Analysis of Deployable Thin Shells with Cutouts (Doctoral dissertation, California Institute of Technology).

Ferraro S and Pellegrino S (2018) Self-deployable joints for ultra-light space structures. 2018 AIAA Spacecraft Structures Conference, AIAA–2018–0694.

Ferraro S and Pellegrino S (2019) Topology optimization of composite self-deployable thin shells with cutouts. AIAA Scitech 2019 Forum, AIAA–2019–1524.

Fleck NA and Budiansky B (1991) Compressive failure of fibre composites due to microbuckling. In: Inelastic deformation of composite materials. Springer, pp. 235–273.

Greschik, G. (1996). Deployment of dishes with surface discontinuities. Journal of Spacecraft and Rockets 33(4): 569-574.

Halpin JC and Tsai SW (1969) Effect of environmental factors on composite materials.

Jackson KE, Kellas S and Morton J (1992) Scale effects in the response and failure of fiber reinforced composite laminates loaded in tension and in flexure. Journal of Composite Materials 26(18): 2674–2705.

Jain AK (1989) Fundamentals of Digital Image Processing. Englewood Cliffs, NJ: Prentice Hall.

JPS CM (2017) JPS Technical Reference Handbook. 2200 South Murray Avenue, P.O. Box 2627, Anderson, SC, 29622.

Liu L and Morgan EF (2007) Accuracy and precision of digital volume correlation in quantifying displacements and strains in trabecular bone. Journal of Biomechanics 40(15): 3516–3520.

Mallikarachchi HMYC and Pellegrino S (2011) Quasi-static folding and deployment of ultrathin composite tape-spring hinges. Journal of Spacecraft and Rockets 48(1): 187–198.

Mallikarachchi HMYC and Pellegrino S (2013) Failure criterion for two-ply plain-weave CFRP laminates. Journal of Composite Materials 47(11): 1357–1375.

Mallikarachchi HMYC and Pellegrino S (2014). Design of ultrathin composite self-deployable booms. Journal of Spacecraft and Rockets 51(6): 1811–1821.

Miura, K. and Pellegrino, S. (2020) Forms and Concepts for Lightweight Structures, Cambridge University Press.

Mobrem M and Adams D (2009) Lenticular jointed antenna deployment anomaly and resolution onboard the mars express spacecraft. Journal of Spacecraft and Rockets 46(2): 403–410.

Murphey TW, Francis W, Davis B and Mejia-Ariza JM (2015) High strain composites. 2nd AIAA Spacecraft Structures Conference, AIAA–2015–0942.

Nguyen MH, Vijayachandran AA, Davidson P and Waas AM (2019) Particle toughened interfaces enhance mechanical response of composites. AIAA Scitech 2019 Forum, AIAA–2019–1041.

PATZ MT (2019) PMT-F6 toughened cyanate ester resin system. 4968 Industrial Way, Benicia, CA 94510.

Sakovsky M. and Pellegrino, S (2019) Closed cross-section dual matrix composite hinges for deployable structures. Composite Structures 208: 784-795.

Soykasap O (2006) Micromechanical models for bending behavior of woven composites. Journal of Spacecraft and Rockets 43(5): 1093–1100.

Stock SR (2008) Recent advances in x-ray microtomography applied to materials. International Materials Reviews 53(3): 129–181.

Sutton MA, Orteu JJ and Schreier H (2009) Image correlation for shape, motion and deformation measurements: basic concepts, theory and applications. Springer Science & Business Media.

Tan, L. T. and S. Pellegrino (2006) Thin-shell deployable reflectors with collapsible stiffeners: Part 1 Approach. AIAA Journal 44(11): 2515-2523.

Tan, L. T. and S. Pellegrino (2012). Thin-shell deployable reflectors with collapsible stiffeners: experiments and simulations. AIAA Journal 50(3): 659-667.

Tibbalds, B., Guest, S.D, and Pellegrino, S. (2004) Inextensional packaging of thin shell slit reflectors. Technische Mechanik 24(3-4): 211-220.

Wang ASD, Tung RW and Sanders BA (1980) Size effect on strength and fatigue of a short fiber composite material. Emerging technologies in aerospace structures, design, structural dynamics and materials : 37–52.

Weibull W (1939) A statistical theory of strength of materials. Ingeniorsvetenskapsakademiens, Handlingar 151, Stockholm.

Wisnom MR (1991) Relationship between strength variability and size effect in unidirectional carbon fibre/epoxy. Composites 22(1): 47–52.

Xu F (2018) Quantitative characterization of deformation and damage process by digital volume correlation: A review. Theoretical and Applied Mechanics Letters 8(2): 83–96.

Yee JCH and Pellegrino S (2005) Folding of woven composite structures. Composites Part A: Applied Science and Manufacturing 36(2): 273–278.

Yee, J. C. H. and S. Pellegrino (2005). Composite tube hinges. Journal of Aerospace Engineering 18(October): 224-231.

Zweben C (1981) The effect of stress nonuniformity and size on the strength of composite materials. Journal of Composites, Technology and Research 3(1): 23–26.